ISSN 1999-656X

Iraqi Journal of Applied Physics Letters

VOLUME (4) ISSUE (1) JANUARY-MARCH 2021

Sponsored and Published by
Iraqi Society for Alternative and Renewable Energy Sources and Techniques

Co-published by
American Quality for Scientific Publishing

IRAQI JOURNAL OF APPLIED PHYSICS LETTERS

The *Iraqi Journal of Applied Physics Letters (IJAPLett)* is a peer reviewed journal of high quality devoted to the publication of original research papers from applied physics and their broad range of applications. IJAPLett publishes quality original research letters in physics and its applications in the broadest sense. It is intended that the journal may act as an interdisciplinary forum for physics and its applications. Innovative applications and material that brings together diverse areas of physics are particularly welcome. IJAPLett aims to disseminate knowledge; provide a learned reference in the field; and establish channels of communication between academic and research experts, policy makers and executives in industry, commerce and investment institutions. IJAPLett is a quarterly specialized periodical dedicated to publishing original letters in: Applied & Nonlinear Optics, Applied Mechanics & Thermodynamics, Digital & Optical Communications, Electronic Materials & Devices, Laser Physics & Applications, Plasma Physics & Applications, Quantum Physics & Spectroscopy, Semiconductors & Optoelectronics, Solid State Physics & Applications, Alternative & Renewable Energy, and Environmental Science & Technology.

ISSN (Print): 1999-656X, ISSN (Online): 2958-6488

EDITORIAL BOARD

Editorial Office:
P. O. Box 55259, Baghdad 12001, IRAQ
Website: www.iraqiphysicsjournal.com
Emails: editor@iraqiphysicsjournal.com, editor_ijap@yahoo.co.uk, ijap.editor@gmail.com,

ADVISORY BOARD

SPONSORED BY
IRAQI SOCIETY FOR ALTERNATIVE AND RENEWABLE ENERGY SOURCES AND TECHNIQUES (I.S.A.R.E.S.T.)
P. O. Box 55259, Baghdad 12001, IRAQ

PUBLISHED BY
AMERICAN QUALITY FOR SCIENTIFIC PUBLISHING INC.
1479 South De Gaulle Ct, Aurora,
CO 80018, United States

IRAQI JOURNAL OF APPLIED PHYSICS LETTERS

ISSN (Print): 1999-656x, ISSN (Online): 2309-1673

INSTRUCTIONS TO AUTHORS

CONTRIBUTIONS

Contributions to be published in this journal should be original research letters, i.e., those not already published or submitted for publication elsewhere, communications or letters to editor.
Manuscripts should be submitted to the editor at the mailing address:

Iraqi Journal of Applied Physics Letters, Editorial Board, P. O. Box 55259, Baghdad 12001, IRAQ
Website: www.iraqiphysicsjournal.com
Email: editor@iraqiphysicsjournal.com, editor_ijap@yahoo.co.uk, ijap.editor@gmail.com

MANUSCRIPTS

Two hard copies with soft Word copy on a CD or DVD should be submitted to Editor in the following configuration:

- **One-column** Double-spaced one-side A4 size with 2.5 cm margins of all sides
- Times New Roman font (16pt bold for title, 14pt bold for names, 12pt bold for headings, 12pt regular for text)
- Manuscripts presented in English only are accepted.
- English abstract not exceed 100 words
- 4 keywords (at least) should be maintained on (PACS preferred)
- Author(s) should express all quantities in SI units
- Equations should be written in equation form (*italic* and symbolic) NOT in plain text
- Tables and Figures should be separated from text and placed in new pages after the references
- Charts should be indicated by the software used for generating them (e.g., Excel, MATLAB, Grapher, etc.)
- Figures and diagrams can be submitted in original colored forms for assessment and they will be returned to authors after provide printable copies
- Only original or high-resolution scanner photos are accepted
- For electronic submission, articles should be formatted with MS-Word software.

AUTHOR NAMES AND AFFILIATIONS

It is IJAPLett policy that all those who have participated significantly in the technical aspects of a paper be recognized as co-authors or cited in the acknowledgments. In the case of a paper with more than one author, correspondence concerning the paper will be sent to the first author unless staff is advised otherwise.
Author name should consist of first name, middle initial, last name. The author affiliation should consist of the following, as applicable, in the order noted:
- Company or college (with department name or company division), Postal address, City, Governorate or State, zip code, Country name, contacting telephone number, and e-mail

REFERENCES

The references should be brought at the end of the article, and numbered in the order of their appearance in the paper. The reference list should be cited in accordance with the following examples:
[1] X. Ning, R. Benford and M.R. Lovell, "On the Sliding Friction Characteristics of Unidirectional Continuous FRP Composites", *J. Tribol. Func. Mater.*, 124(1) (2002) 5-13.
[2] M. Barnes, "Stresses in Solenoids", *J. Appl. Phys.*, 48(5) (2001) 2000–2008.
[3] J. Jones, **"Contact Mechanics"**, Cambridge University Press (Cambridge, UK) (2000), Ch.6, p.56.
[4] Y. Lee, S.A. Korpela and R. Horne, "Structure of Multi-Cellular Natural Convection in a Tall Vertical Annulus", Proceedings of 7th International Heat Transfer Conference, U. Grigul et al., eds., Hemisphere (Washington DC), 2 (1982) 221–226.
[5] M. Hashish, "Waterjet Technology Development", High Pressure Technology, PVP-Vol. 406 (2000) 135-140.
[6] D.W. Watson, "Thermodynamic Analysis", ASME Paper No. 97-GT-288 (1997).
[7] C.Y. Tung, "Evaporative Heat Transfer in the Contact Line of a Mixture", Ph.D. thesis, Rensselaer Polytechnic Institute, Troy, NY (1982).

PROOFS

Authors will receive proofs of papers and are requested to return one corrected copy as a WORD file on a compact disc (CD) or by email. New materials inserted in the original text without Editor's permission may cause rejection of paper unless the handling editor is informed.

COPYRIGHT FORM

Author(s) will be asked to sign the IJAPLett Copyright Form and hence transfer copyrights of the article to the Journal soon after acceptance of it. This will ensure the widest possible dissemination of information.

OFFPRINTS

Authors will receive electronic offprint free of charge and any additional reprints can be ordered.

SUBSCRIPTION AND ORDERS

Annual fees (4 issues per year) of subscription are:
50 US$ for individuals inside Iraq; **200** US$ for institutions inside Iraq;
100 US$ for individuals abroad; **300** US$ for institutions abroad.

Computer-Controlled Biogas Production from Organic Waste

Qutaiba M.H. Ali, Shareef F.S. Al-tikrity

Department of Physics, College of Science, Tikrit University, Tikrit, IRAQ

Abstract

The advanced system of (AD) was designed to generate biogas using organic waste. The system consists of an entering, cutting and mixing unit for waste and water, a fermentation unit with a capacity of 2000 liters and a gas storage unit. The fermentation process is controlled by programming the temperature , the methane gas and the pH sensor connected to the system. The gas was generated from household waste by mixing with water and fermenting it for a period time up to 25 days. The highest amount of gas was during the 17th day from the time of retention. The total amount of gas produced by the system is approximately 60 liters. System waste from the fermentation process can be used as an organic fertilizer. The system is designed with suitable specifications for home use, ease of maintenance and to meet renewable energy. The system was controlled completely by computer.

Keywords: Alternative energy; Anaerobic digestion; Organic waste; Methane gas
Received: 2 July 2020; **Revised:** 20 July 2020; **Accepted:** 19 November 2020; **Published:** 1 January 2021

1. Introduction

The main source of energy is fossil fuels and the combustion process causes problems of atmospheric pollution. Waste energy is ideal and renewable because it can be converted to non-polluting into biogas that can be used as environmentally friendly biofuels [1]. The perspective of solid waste has dramatically changed with increasing population and economic development, therefore, the effects of climate change must be mitigated and the transition from fossil fuels to renewable energy must be accelerated. The process of waste treatment can generate clean energy, whether electric or thermal, and it also touches on the idea of waste disposal, which is considered as a waste management option [2]. Biogas is capable of alleviating growing concerns about the energy crisis and climate change as well as reduce dependence on fossil fuels. Biogas can be produced from organic waste, consisting mostly of methane (CH_4) and carbon dioxide (CO_2), used to generate thermal energy, and considered as a light fuel that releases less CO_2 into the atmosphere during combustion [3]. Biogas is produced by decomposing and breaking down organic materials into their basic organic components, where methane bacteria are used to ferment and decompose these materials under special conditions under anaerobic conditions and at appropriate temperature rates [4]. There were many designs for biogas production systems, although, they were primitive and containing obstacles that led to their failure. Such obstacles – ignored in the system design – are the weak construction skills and the lack of use of appropriate materials in manufacturing. As well, most designs need to be drilled in the ground [5], which is not suitable in rocky terrain and with difficult maintenance and cleaning, where they need to be cleaned every period and have a short life . In addtion, there are other defects in such designs that are not tightly closed, which leads to a leak in the gas. In this work, a system that addresses all these problems and defects is designed and manufactured to show the ease of manufacture, security, and transportability, as well as an advanced control of the anaerobic digestion process in terms of follow-up through the sensors connected to it that makes the whole system controlled by computer. The best biogas production can be obtained and the remnants of materials can be used after the

anaerobic digestion process as organic fertilizer.

Many different technologies are used to treat waste from the organic portion of household waste. These systems vary depending on the reactor design and operating parameters. Reactor design depends on the raw materials to be processed, while the digester design depends on the amount available of raw materials, which determines the actual capacity of the reactor to produce [6].

While designing the biogas production system, the factors that will affect the anaerobic digestion process within the system must be taken into accounts, such as temperature, pH, and loading rate of organic waste. In our study, these were taken into account and can be classified as follows:

The pH of biomass within the digester is one of the factors affecting the digestion of organic waste, where the methane-producing bacteria are affected by the change in pH and affecting the bacterial growth and the rate of methane gas production in the anaerobic digestive reservoir. In this study, it was observed that the best amount of biogas production in the anaerobic digester is achieved when the pH value is 7.5-6.5. The retention period and amount of organic waste inside the digester affect the pH amount [7]. Figure (1) shows the variation in pH value with the retention time.

Temperature is one of the factors that affects the process of anaerobic digestion within the digestive unit and has a role in determining the amount of biogas production, as it is a prerequisite for optimal survival and growth of microbial concentrations. Although, the digester can operate at different temperatures, methane bacteria have two temperature levels, representing a thermophilic level as it reacts at high temperatures up to 25-40°C and medium-temperature bacteria that work within 50-65°C [8].

The biomass loading rate determines the amount of organic waste that can be introduced into the anaerobic fermentation tank and represents an indicator for measuring the biodegradable capacity of the anaerobic digestion unit. The amount of produced biogas decreases when there is an overloading of organic waste in the anaerobic digestion unit due to the accumulation of fatty acids in the digester that inhibits the process of anaerobic digestion [9]. Therefore, specific ratios of organic materials with water were adopted to reach the best production of gas and to get rid of the inhibitors in anaerobic fermentation process.

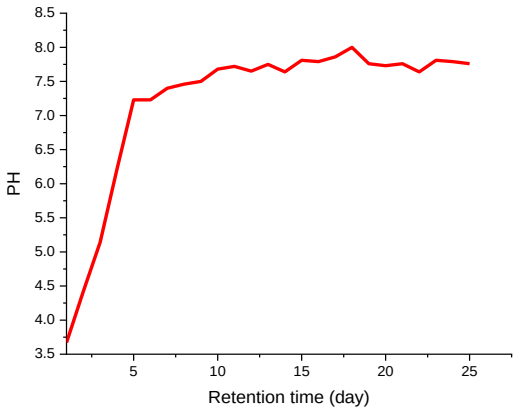

Fig. (1) Variation of pH value during the retention time

2. Materials and Methods

An effective and advanced model was designed to take into account all obstacles, defects and errors in previous designs in order to reach the best model design. As well, the reasons that affect the anaerobic digestion (AD) process were studied to reach the best design and highest productivity of biogas. Factors affecting the anaerobic fermentation process were followed up through sensors connected to the Arduino program to control the anaerobic digestion unit. Table (1) shows the design parameters of the biogas generating unit.

It is an airtight tank designed in the form of a cylindrical with an operating capacity of 2000 liters and the thickness of the zinc-galvanized iron plates chosen for the manufacture of the fermentation tank was 1.6 mm. This tank is very durable for difficult stressful work while all tanks of other anaerobic digestion designs are made of fiber-reinforced plastic, which are well tolerated for external conditions. Also, this type of iron provides protection against corrosion and salts

and is easy to manufacture the shape required for the design. The dimensions of the cylindrical tank to provide sufficient surface area for the fermentation process are 2m in length and 50cm in radius with total volume of 6.28 m^3.

Table (1) Design parameters of the Biogas unit

Design parameters	Value
Fermentation tank capacity	2000 L
The thickness of the iron sheets used in the design	1,6 mm
Fermentation tank length	200cm
Fermentation tank radius	50cm
The diameter of the outlet hole of the digestion unit	10cm
Inlet pipe length	100cm
Shredder tank length	50 cm
Shredder tank diameter	37cm
gas tank length	60cm
Gas tank diameter	40cm

This unit is designed on the side of the fermentation tank as an output hole with a diameter of 10 cm containing a tight lid that can be closed and opened. This hole is used for emptying at the end of the fermentation process, to take out the remnants of waste after decomposition through it and to facilitate the cleaning process. It was placed in a suitable place at the bottom of the fermentation tank so that the remaining biomass comes out with ease. The hole was placed at an appropriate height from the ground due to the presence of iron bases installed on the fermentation tank.

This is inlet hole designed from the top in order to enter the biomass easily and a cylindrical pipe with a diameter of 10 cm and a length of 100 cm was welded cut from the bottom direction of the ellipse while the other side is serrated in order to put it on the PVC plastic valve. This hole contains a valve to provide an advantage to control the closing and opening of the pipe when needed.

It is a tank designed to mix biomass with water before entering the fermentation tank, where the mixing tank is cylindrical in shape with a diameter of 37cm and a height of 50 cm, from the bottom it is connected to the inlet hole valve and carried by a base designed to carry the mixing tank and installed at the top of the cutting motor, where a motor containing a cutting blade was installed on it in order to cut and mix the biomasses, and this facilitates the decomposition process during the fermentation process, and there is also a tank of water A numbered next to the fermentation tank supplies the tank with water according to the amount that is determined during mixing, and there is a base that holds this tank.

It is a closed cylinder has been manufactured two holes for gas valves the first valve is located at the bottom of the gas tank and is linked with the fermentation tank with a PVC tube and the second valve is located at the top of the tank and the valve is connected to a rubber balloon that expands when there is biogas production and to avoid excessive pressure on the gas filling tank as well as the gas valve can be closed and the gas system separated when the filling is completed.

3. Results and discussion

In order to test the treatment unit that was manufactured, 140 kg of organic waste was placed with 280 kg of water and the quantity was placed in the form of parts in the cutting tank in order to be mixed well and stirred to ensure the dispersion of the worn parts of the organic waste and achieve a homogeneous mixture and then we open the valve to enter the mixture inside the fermentation tank and close it well and the retention period was 25 days and the amount of cumulative biogas production was about 60 liters and the pH rate was controlled During the fermentation process and it was between (7.3-7.7) and that the temperature was between (42°C-46°C) for the fermentation process. Finally, it can be said that the results obtained can be represented in the Fig. (8), which shows the amount of biogas production (ml/day), which was obtained during the fermentation processes and in different retention periods and within 25 days. This amount of biogas produced from the manufactured digestion unit is very good and will be useful as renewable energy and an alternative to fossil fuels. This system is considered an experimental system that can be used to conduct many biogas researches. Where all the electronic parts were connected by the Arduino board for the temperature sensor. In

addition, all the activities in the system were controlled by the computer.

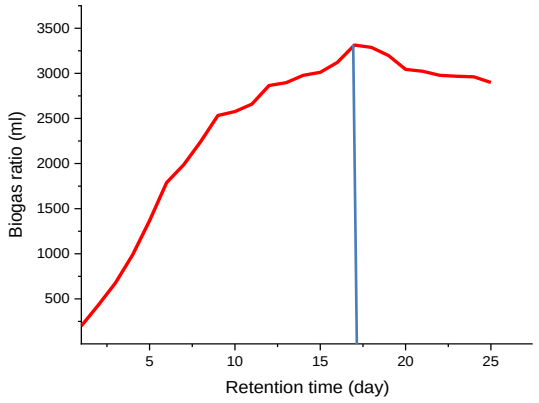

Fig. (8) The proportion of biogas produced (ml/day) for each day of the retention time

4. Conclusion

In this research we presented the design and manufacture of an anaerobic digester unit for biogas generation and the materials selected in the manufacture of the digester were effective as they meet practical needs (AD). The design meets all previous studies for the production of biogas and taking into account all the factors affecting the digestion process and treating it by design in terms of the effect of external temperatures and insulation of the manufactured materials, including the fermentation tank, as well as adding a cutting tank to untie the biomasses, cutting them and mixing them with water, in addition to controlling the digestion process and following it up electronically through sensors related to the digester, and taking into account the choice of material availability for everyone as well as its cheapness. The typical design of the manufactured unit gives additional advantages in terms of longer life, high durability, ease of cleaning and maintenance. This manufactured unit is highly recommended due to its low operating costs and special features such as manufacturing costs and ease of use. In addition, manure will also be produced as a by-product.

References

[1] A. Rafiee, K. R. Khalilpour, J. Prest, and I. Skryabin, "Biogas as an energy vector," *Biomass and Bioenergy*, vol. 144, p. 105935, 2021.

[2] C.-Y. Lin and H.-P. Chen, "Sulfate effect on fermentative hydrogen production using anaerobic mixed microflora," *Int. J. Hydrogen Energy*, vol. 31, no. 7, pp. 953–960, 2006.

[3] H. M. Zabed, S. Akter, J. Yun, G. Zhang, Y. Zhang, and X. Qi, "Biogas from microalgae: Technologies, challenges and opportunities," *Renew. Sustain. Energy Rev.*, vol. 117, p. 109503, 2020.

[4] A. Schnürer, "Biogas production: microbiology and technology," *Anaerobes Biotechnol.*, pp. 195–234, 2016.

[5] G. Crini and E. Lichtfouse, "Advantages and disadvantages of techniques used for wastewater treatment," *Environ. Chem. Lett.*, vol. 17, no. 1, pp. 145–155, 2019.

[6] M. Mel, A. S. H. Yong, S. I. Ihsan, and R. H. Setyobudi, "Simulation study for economic analysis of biogas production from agricultural biomass," *Energy Procedia*, vol. 65, pp. 204–214, 2015.

[7] A. E. Cioabla, I. Ionel, G.-A. Dumitrel, and F. Popescu, "Comparative study on factors affecting anaerobic digestion of agricultural vegetal residues," *Biotechnol. Biofuels*, vol. 5, no. 1, pp. 1–9, 2012.

[8] S. P. Lohani and J. Havukainen, "Anaerobic digestion: factors affecting anaerobic digestion process," in *Waste Bioremediation*, Springer, 2018, pp. 343–359.

[9] A. Anukam, A. Mohammadi, M. Naqvi, and K. Granström, "A review of the chemistry of anaerobic digestion: Methods of accelerating and optimizing process efficiency," *Processes*, vol. 7, no. 8, p. 504, 2019.

Mechanical Characterization of Small Sized Bladed Wind Turbine under Low Wind Speed

Othman K. Zidane, Yaseen H. Mahmood

Department of Physics, College of Science, University of Tikrit, Tikrit, IRAQ

Abstract

In this paper, a small horizontal wind turbine rotor blade is designed to operate under low wind speed, it is well known that the design of the rotor blade is a difficult task due to the calculations involved in the design process. The Q-Blade program was used to design and simulate the turbine rotor blade during working conditions, with some engineering improvements to the shape of the blade by distributing the airfoils along the blade and controlling the airfoil chord length and twist angle using the blade element theory (BEM). Where airfoil (NACA7611) was used for a three-blade rotor and a five-blade rotor based on the turbine type and rotor size to generate mechanical power from wind power. Comparison and analysis (turbine power, power coefficient, torque coefficient) were carried out at low wind speed (2-7m/s) and highly accurate results were obtained. Also, it was found that the best performance in which a three-bladed turbine rotor can work with a turbine power of 3.951 kW and a power coefficient of 0.43. Also, the power of the turbine was obtained 4.757 kW, and the power coefficient of 0.51 for the five-blade rotor. These values do not exceed the Betz limit (0.59%), which is good efficiency for a small wind turbine. It was found that the design of a small horizontal wind turbine with five blades is better than a turbine with three blades and is suitable for working in areas with low wind speed, and with high efficiency compared to the size of the turbine.

Keywords: Wind Energy; Blade of Wind Turbine; Power Coefficient; Torque Coefficient; Low wind speed
Received: 10 August 2020; **Revised:** 12 September; **Accepted:** 19 September; **Published:** 1 January 2021

1. Introduction

Industrial growth in countries is related to their energy resources, the use of oil, hydrocarbons, and coal, which was the main source of energy production in the past, has a significant impact on the environment. Therefore, at present, some developed countries are turning to use alternative energy to reduce Environmental pollutants, such as the use of hydro, solar, and wind energy. Wind energy is one of the clean and preferred energies for some countries, and the energy that is produced by wind turbines depends on the blade engineering and wind speed, since wind speed varies in time and place and according to geographical location, this led to the use of small wind turbines on the roofs of buildings, which are characterized by its low cost, due to the small size of the turbine, as the cost, increases with the increase in the number of blades and vice versa for wind turbines with a small number of blades also, one of the advantages of small-sized wind turbines is simple structure and low noise in addition to its versatility make it a preferred choice for many and a reliable source [1,2]. A horizontal axis wind turbine is designed being a clean source of energy, there are no hazards to electricity production by a wind turbine. These turbines neither emit any toxic nor have any specific productivity time, making these a superior alternative to fossil fuels and solar power. The wind turbine is analytically designed and then the results were verified using simulation (Q-blade) software. A theoretical efficiency of 38.25% was obtained as the simulation results determined a power of 750-800 W at an average wind speed of 4-8.5m/s [3]. New and effective airfoils were developed for small-sized horizontal axis wind turbine rotor blades using blade element theory and momentum theory, and calculations were carried out using the Q-Blade program and ANSYS CFX program and they reached a power of 1kW at a wind speed of 8.4 m/s [4]. A horizontal wind turbine was designed using a NACA 4412 airfoil and a five-blade rotor with a diameter of 1.4 m with a change in wind speed 2-6m/s. Where the aerodynamics of the blade was analyzed

based on the blade element theory (BEM), which refers to parsing each section of the blade independently from the other. So that the results of the blade sections are combined as a function of the blade geometry, and using the Q-blade program, it was found that the energy of the wind turbine increases with the increase in wind speed based on the increase in the value of TSR in addition to the increase in the power factor as the wind speed increases [5]. Helical blades, horizontal wind turbines, were designed for urban electric power generation and it was concluded that such turbines produce (RPM) at wind speed 5m/s, and to get the best power output the wind speed should be 18-25 m/s and that this design withstands wind disturbances and enjoys a high efficiency of up to 80% of the energy available in the wind and at low altitudes [6]. A flexible blade design technology study was conducted for the Savonius-type vertical axis wind turbine (VAWT). So that the shape of the blade changes due to the inertial forces of the blade during rotation or due to aerodynamics, and by comparing it with the blades of classic wind turbines, it was found that the new design led to an increase in the power coefficient (C_P) by 8% and the tip speed ratio (TSR) high and that The system has achieved good efficiency compared to traditional blades. That is, the shape of the blade must be improved to suit the wind speed in the geographical location and not rely on a traditional shape or design [7].

3. Rotor Design

The first step in designing a wind turbine is to choose the most suitable airfoil for the turbine rotor blade, where a high-lift coefficient and low-drag flap is chosen at low wind speeds to achieve the best power coefficient (C_P), and obtain an effective and intuitive design for the turbine rotor, Q-Blade software was used, to design the blade, and make some engineering improvements to the shape of the blade by distributing the airfoils along the blade and controlling the airfoil chord length and twist angle using the blade element theory (BEM), where the airfoil (NACA 7611) was selected based on the type of turbine and the size of the rotor to generate mechanical energy from wind energy (Fig. 2).

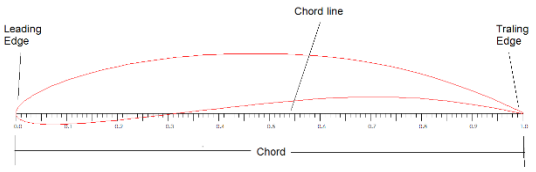

Fig. (2) The shape of the airfoil, which was chosen for the rotor blade design

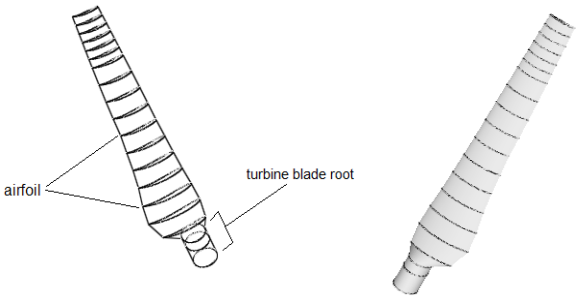

(a) **(b)**

Fig. (3) The design of the blade (a) shows the distribution of the ailerons along the length of the blade. (b) The final blade shape

Table (1) Horizontal axis wind turbine rotor specifications

No.	Position (cm)	Chord (cm)	Twist-angle (deg)	Foil
1	0	10	0	Circular foil
2	10	10	0	Circular foil
3	15	10	0	Circular foil
4	20	18.7	14.2	NACA7611
5	30	22.7	13.8	NACA7611
6	40	21.4	13.4	NACA7611
7	50	19.1	13	NACA7611
8	60	17.6	12.6	NACA7611
9	70	16.5	12.2	NACA7611
10	80	15.4	11.8	NACA7611
11	90	15.1	11.4	NACA7611
12	100	14.3	11	NACA7611
13	110	14.3	10.6	NACA7611
14	120	13.3	10.2	NACA7611
15	125	12.9	10	NACA7611
16	130	12.5	9.8	NACA7611
17	135	12.1	9.6	NACA7611
18	140	11.7	9.4	NACA7611
19	145	11.3	9.2	NACA7611
20	150	10.8	9	NACA7611

The second stage of the design is to divide the blade, which has a length of 150 cm, into 20 sections, and use the first three sections as the root of the blade, and 17 of the other sections as the airfoils (NACA 7611) are distributed on it Table (1), so that the airfoil is larger in the parts close to the root and smaller in the outer sections of the blade, where the length of the airfoil (NACA 7611) near the root is 18.746 cm and at the tip of the blade is 10.898 cm long, and the twist angle is

distributed from 14.2° at the root of the blade to 9° at the tip of the blade.

4. Results and Discussion

After completing the design process and making some appropriate modifications to the shape of the blade, a simulation was conducted to find out the mechanical properties (turbine power, power coefficient, torque coefficient), to perform the rotor blades, whether the design can be used in practical applications or not, where an analysis of the turbine rotor was conducted wind, with three blades, and five blades, to find out which one is better for producing power and which one works to generate mechanical power at a wind speed rate of 2-7m/s, and using Eq. (2) approved in the analysis program Q-blade, at a low wind speed, it was found that the power of a five-bladed turbine increases with the increase in wind speed with greater power than a three-blade turbine. Where the power of the turbine with three blades 3.951 kW and five blades 4.757 kW. Figure (5) shows the difference in the increase in the mechanical power of the turbine gained from the wind. Thus, it can be said that the power of a small wind turbine can be increased by increasing the number of blades, without The need to change the diameter of the rotor to capture wind energy, as the performance of the wind turbine is more sensitive to changes in wind speed whenever the number of blades is more, in a way that suits the size of the turbine, which is coincident with [17]. The choice of the number of blades is important because it directly affects the speed and efficiency of the wind turbine, as the energy gained by the turbine from the wind is proportional to the area swept by the turbine rotor blades. Thus, the number of blades affects on power generation, and the greater the number of blades, the greater the torque of the turbine rotor. In addition to easier rotation at low wind speed, provided that the number of blades is appropriate to the size of the turbine, and by comparing the three-blade turbine and the five-blade turbine, we note that the five-blade turbine, improves performance significantly in areas where the wind speed does not exceed 7 m/s, compared to the traditional three-blade turbine. In addition to the turbine's self-operating, on the other hand, the turbine rotor blade has an unbalanced torsional force acting on the shaft and this undesired deflection may reduce the energy produced and may lead to vibrations. The three-blade turbine has minimal vibration.

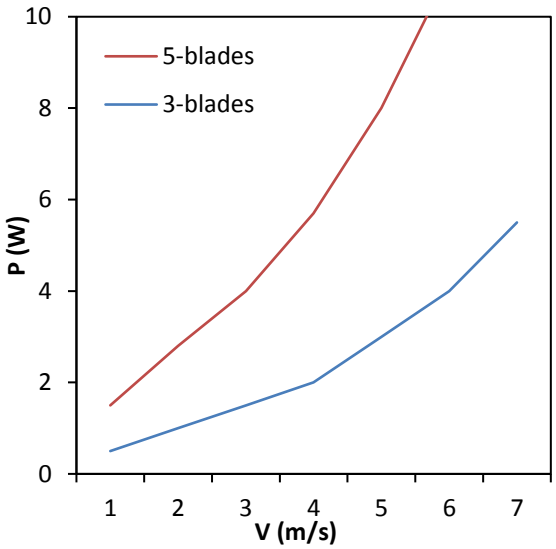

Fig. (5) The power of the turbine with wind speed

5. Conclusions

In this paper, a horizontal axis wind turbine was designed with a rotor consisting of three blades and five blades, and a comparison was made to find out which of the two turbines is better at average wind speed 2-7m/s, to generate mechanical energy from wind energy based on the (BEM) theory using the Q-blade design software, The results of the study showed that using a curved airfoil for the central geometric line the middle line, is better for the blade of a small wind turbine to achieve a lifting force that rotates the turbine rotor.

References

[1] N. Nazir and A. Javed, "Comparison of 1kW Horizontal Axis Wind Turbine Rotor Blade Performance Using Numerical Simulation," 2019 Sixth Int. Conf. Aerosp. Sci. Eng., 2019.

[2] N.P. Noronha and M. Krishna, "Design and analysis of micro horizontal axis wind turbine using MATLAB and QBlade," Int. J. Adv. Sci. Technol., 29(10S) 8877–8885, 2020.

[3] N. Vaidya and S.B. Barve, "Design, Modelling and Comparative Analysis of a Horizontal Axis Wind Turbine. In Soft Computing in Materials Development and its Sustainability in the Manufacturing Sector," CRC Press, 223-229, 2021.
[4] M.R. Birajdar and S. A. Kale, "Performance Analysis of New Airfoils and Blade for a Small Wind Turbine," 24(1) 75–85, 2016.
[5] A.S. Samosir and A. Riszal, "The effect analysis of wind speed variation to the horizontal axis wind turbine design with Q-blade," IOP Conf. Ser. Mater. Sci. Eng., 1173(1) 012009, Aug. 2021.
[6] Y. Patil, "Design, fabrication and analysis of Fibonacci spiral horizontal axis wind turbine," Int. J. Aerosp. Mech. Eng., 5(1) 1–4, 2018.
[7] I. Marinić-Kragić, D. Vučina, and Z. Milas, "Concept of flexible vertical-axis wind turbine with numerical simulation and shape optimization," Energy, 1–28, 2018.
[8] M.B. Pramod, C.P. Srirang, M.B. Sushilkumar, "Experimentation on design and development of mini wind turbine", Int. J. Innov. Technol. Explor. Eng., 8(11) (2019).
[9] H. Muhsen, W. Al-kouz and W. Khan, "Small Wind Turbine Blade Design and Optimization," Symmetry (Basel), 1–14, 2020.
[10] A. Bouanani, M. Bouchaour and L. Merad, "Modeling and Simulation of the Vertical Axis Wind Turbine by Qblade Software," Alger. J. Renew. Energy Sustain. Dev., 2(2) 181–188, 2020.
[11] R. Kumar et al., "Analytical analysis of Carbon-Fiber Composite Material on Horizontal axis wind turbine blade using ANSYS," Int. J. All Res. Educ. Sci. Methods, 9(5) 1025–1035, 2021.
[12] R.I. Jabbar, "Statistical analysis of wind speed data and assessment of wind power density using Weibull distribution function (case study: four regions in Iraq)", in IOP J. Phys.: Conf. Ser., 1804(1) 012010, 2021.
[13] A. Suresh and S. Rajakumar, "Design of small horizontal axis wind turbine for low wind speed rural applications", Mater Today: Proc., 23 (2020) 16-22.
[14] S. Raut et al., "Simulation of micro wind turbine blade in Q-blade", Int. J. Res. Appl. Sci. Eng. Technol., 5(4) (2017) 256-262.
[15] B. Wen et al., "On the power coefficient overshoot of an offshore floating wind turbine in surge oscillations", Wind Energy, 21(11) (2018) 1076-1091.
[16] A. Marashli et al., "Review of Effect of Specific Geometrical Parameters on the Performance of Small Straight Blade–Vertical Axis Wind turbine (SB-VAWTs) of Darrieus-type", Int. J. Renew. Energy Res., 11(4) (2021) 1924-1925.
[17] M.M.M Alaskari, "Experimental Investigation and Performance Simulation of Kit Horizontal Axis Wind Turbine", Int. J. Comput. Appl., 180(16) (2018).
[18] D.H.M. Arán, Y. Tian and S.A. Kinnas, "Effect of wake alignment on turbine blade loading distribution and power coefficient", J. Offshore Mech. Arct. Eng., 141(4) (2019).
[19] A. Eltayesh et al., "Experimental and numerical investigation of the effect of blade number on the aerodynamic performance of a small-scale horizontal axis wind turbine", Alex Eng J., 60(4) (2021) 3931-3944.

XRD Analysis and Structural Properties of Nickel-Doped Zinc Ferrite

Najat A. Dahham, Abdulsamee F. Abdul Aziz, Omar F. Fouad

Department of Physics, College of Science, University of Tikrit, Tikrit, IRAQ

Abstract

Nickel ferrite ($Ni_{0.6}Zn_{0.4}Fe_2O_4$) nanoparticles were synthesized using co-precipitation method. The x-ray diffraction (XRD) pattern was used to determine the structure of $Ni_{0.6}Zn_{0.4}Fe_2O_4$ nanoparticles The details of the surface morphology of $Ni_{0.6}Zn_{0.4}Fe_2O_4$ nanoparticles were obtained by scanning electron microscopic analysis (SEM). The particle size of the $Ni_{0.6}Zn_{0.4}Fe_2O_4$ nanoparticles could be determined by XRD also the anther parameter was determine from the lattice constant (a) and theoretical density ($\rho_{x\text{-}ray}$).

Keywords: Nickel ferrite; Zinc ferrite; Nanoparticles; Lattice constant, Structural properties
Received: 2 March 2020; **Revised:** 5 August 2020; **Accepted:** 12 August 2020; **Published:** 1 January 2021

1. Introduction

Due to its diverse and unique structural, spectroscopic, and magnetic features, spinel ferrite has been produced by a significant number of researchers and scientists in recent years [1]. Microwaves [2], drug delivery [3], gas sensors [4-5], and electronic devices [6] are only a few of the uses for spinel ferrites, all of which are related to the type of transition metals in their network [7]. For their technological uses, low porosity, high density, and species microstructure are necessary [8]. The ferrite nanopowders under investigation crystallize into spinel. The octahedral or tetrahedral positions are occupied by the divalent A and trivalent B cations, respectively, depending on their lattice surroundings. Depending on how they are distributed, the spinel ferrites are divided into two categories of M^{2+} and Fe^{3+} cations on (A) or [B] sites: normal spinel AB_2O_4 with the formula $(A^{2+})A[Fe^{3+}Fe^{3+}]BO^{2-}$, and the inverse type B (AB) O_4 with the formula $(A^{2+}Fe^{3+})A[A^{2+}Fe^{3+}]BO^{2-}$ [9]. Figure (1) shows that spinel ferrites crystallize [10], and because the radius of the metal ion is smaller than the radius of the oxygen ions, it is trapped between the two oxygen ions.

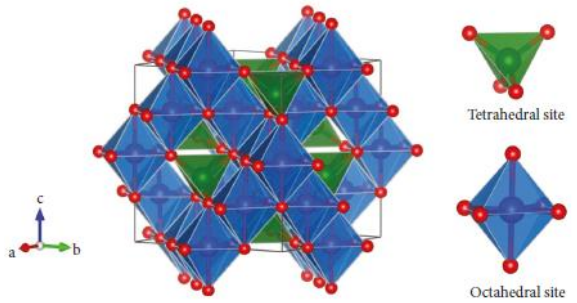

Fig. (1) The cubic spinel structure. Oxygen locations are shown in red, while the tetrahedral (A-site) and octahedral cation (B-site) are indicated in green and blue, respectively

The structural and magnetic characteristics of spinel ferrites are affected by the cation occupancy along the (A) and [B] sites. Because of its usual characteristics, decreased eddy current losses, low conductivity, and good electrochemical stability, nickel ferrite is one of the versatile and technologically significant soft ferrite materials that is ferromagnetic [11]. Due to their high magnetic permeability, low electrical conductivity, and excellent performance at high frequencies, Ni-Zn spinel ferrites are remarkably intriguing [14]. A variety of techniques, such as the hydrothermal approach [15], co-precipitation [16], sol-gel [17], microwave combustion [18], and others [19-20], were utilized to create the Ni-Zn Nano ferrite. The sol-gel technique is one of

these methods that is both practical and efficient. Chemical homogeneity, high purity, and energy savings have all been accomplished with success using the sol-gel technique [21]. For Ni-Zn ferrites, microscopic features include factors like composition, grain size, dopant quantity, impurities, production process, and heating conditions. [22].

2. Experimental details

To prepare the compounds used in experimental by chemical precipitation method, iron nitrate, zinc nitrate and nickel nitrate were dissolved in (100ml) of distilled water using a magnetic stirrer (Stirrer magnetic) at a temperature of (60°C) and for half an hour in order for the substance to be completely and homogeneously dissolved in water, then all the solutions are mixed in a glass flask at a temperature of (60°C) for half an hour with continuous stirring by means of the magnetic mixer.

As for the second stage, (40g) of sodium hydroxide (NaOH) was dissolved in (200 ml) of distilled water in a glass flask with continuous stirring using a magnetic mixer at a temperature of (60°C) for 15 minutes. Sodium hydroxide solution is used as a precipitating agent and to determine the pH value.

As for the third stage, it included mixing all the solutions in a glass flask at a temperature of (60°C) for half an hour with continuous stirring by means of the magnetic mixer. Then we distill the sodium hydroxide solution mixture by a burette slowly over the solution of the mixture of solutions while continuing the mixing process at a temperature (60°C) until the sodium hydroxide solution is distilled to determine the pH value.

After completing the distillation process, the solution will be clear with a pH that we determine. This solution is filtered with filter paper and then washed several times with distilled water to get rid of insoluble nitrates. Then the resulting substance is taken and dried in a drying oven at a temperature (100°C) to obtain a dry, moisture-free compound. Then the powder we obtained is calcined at a temperature of (700°C) for two hours

3. Results and Discussion

The ferrite samples were prepared based on the molar concentration and molecular weights by comparing the X-ray diffraction patterns of ferrite after sintering at a temperature of 700°C and in comparison with the standard labels it was found that they are identical to the standard label number (JCPDS 8-324). And as shown in Fig. (2), and from the X-ray diffraction pattern of the sample, the appearance of peaks (220), (311), (222), (400), (422), (333), (440) and (533) within the angular range (20°-80°) for all the compounds prepared by chemical precipitation method, where the peaks are considered dominant, which refers to the geometric crystal structure of ferrite powder and from the shape of the diffraction spectrum, the appearance of the spin phase of zinc [88]. No impurities were found for any other material, which proves that the material has a very high purity. A variation in intensity was found where the highest intensity was due to the (311) peak corresponding to the angle 35.7°, when looking at the spectrogram We notice an increase in the intensity of the peaks with increasing pH, which leads to the formation of nanoparticles of varying size according to the pH value. As the pH increases, the granular size increases [89]. The ferrite compound with the formula $Ni_{0.6}Zn_{0.4}Fe_2O_4$ and pH values was prepared, (pH = 1.5, 7, 10, and 13) we find that the granular size has reached the value 18-48nm of the pH value, respectively, and the reason for the increase in size is The granularity of ferrite materials is due to the fact that magnetic materials tend to agglomerate, which leads to the increasing of particles with each other, which leads to an increase in the surface area of the material, thus increasing the granular size. We can also justify this increase due to the recrystallization that reduced the amplitude of the lattice constant [90].

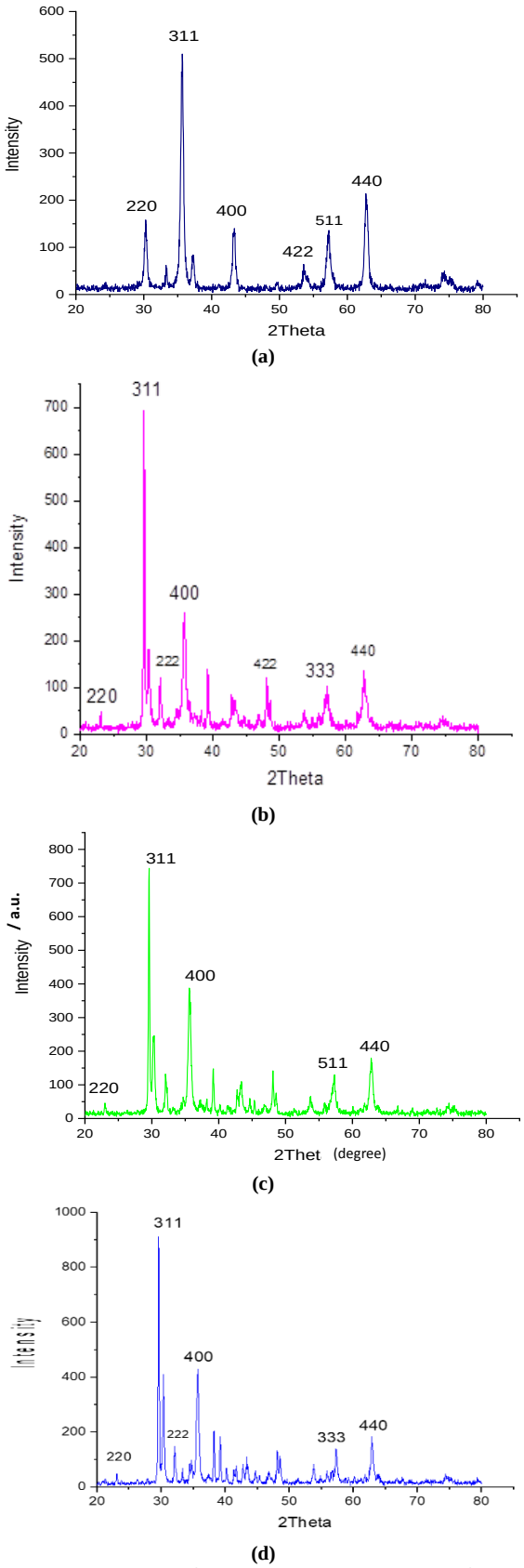

Fig. (2) XRD patterns of $Ni_{0.6}Zn_{0.4}Fe_2O_4$ with pH value of (a) 1.5, (b) 7, (c) 10, and (d) 13

The lattice constant based on Miller's coefficient for the highest obtained intensity and for the peak (311), which was prominent in terms of intensity, location and granular size. It increased with the increase of the pH and also with the increase in the content of the zinc ion whose value was different between the two formulas, as it causes the increase to the migration of the triple iron ion from the tetrahedral sites to the range of the octahedral sites [23].

The theoretical density, where it was found that the theoretical density decreased with increasing pH and also with an increase in the zinc ion content, where the ratios varied between 5.32-5.42g/cm^3, where in the ferrite spinel structure, which contains the tetrahedral and octahedral structure, it is preferred to occupy the eight-surfaced corners with Zn^{2+} ions because of the predominance of volume over mass and also because the diameters of the ions are not the same size [24].

Table (1) Values of lattice constant with pH for (311) peak

pH value	Lattice constant a (Å)
7	**8.382**
10	**8.391**
13	**8.373**

Table (2) Values of theoretical density at different pH values

pH value	Theoretical density ($\rho_{x\text{-}rd}$) (g/cm^3)
7	**5.25**
10	**5.384**
13	**5.342**

Reference

[1] W.D. Kingly, D.R. Uhmann and H.K. Bowen, **"Introduction to Ceramic"**, 2nd ed., John Wiley & Sons (NY, 1976).
[2] P.I.B. Clarricoats, **"Microwave Ferrites"**, Chapman & Hall Ltd. (London, 1961).
[3] C. Kittle, **"Introduction to Solid State Physics"**, 5th ed., John Wiley & Sons (NY, 1976).
[4] K.J. Standley, **"Oxide Magnetic Materials"**, 2nd ed., Clarendon Press (Oxford, 1972).
[5] L.L. Hench and J.K. West, **"Principle of Electronic Ceramic"**, John Wily & Sons (1990).
[6] M.M Eltabey, W.R. Ajami and H.T. Mohsen, "Improvement of the magnetic properties for Mn-

Ni-Zn ferrites by rarearthe Nd^{2+} ion substation", J. Adv. Res., 5 (2014) 601-605.
[7] V.A. Goel et al., "High resistivity nickel-zinc ferrites by the citrate precursor method", J. Magnet. Mater., 192 (1999) 271-276.
[8] G.H. Jonker and A.L. Stuijts, "Controlling the properties of electroceramic materials through their microstructure", Philips Tech. Rev., 32(3/4) (1971) 79-95.
[9] A.L. Stuijts and C. Kooy, "Influence of Technological Factors on the Sintering Behavior of ferrite", in Proc. Conf. held under the auspices of British Cer. Soc. and the Netherlands Keramische Vereniging at Noordwijk an Zee 13-17 May, 1963, in Science of Ceramic, edited by G.H. Stewart, v2 (1965).
[10] Y. Chien and Y. Chaoko, "The effect of silica characterization on the microstructure of $BaFe_{12}O_{19}$ ferrites", J. Mater. Sci., 25(3) (1990) 1711-1714.
[11] A. Vijayakalakhmi and N.S. Gajbhiya, "Magnetic properties of Single domain $SrFe_{12}O_{19}$ particles synthesized by citrate precursor technique", Appl. Phys., 83(1) (1998) 400.
[12] G.A. Hossienpour et al., "Electromagnetic properties and microwave absorbing characteristics of doped barium hexaferrite", J. Magnet. Mag. Mater., 302 (2006) 429-435.
[13] R. Richa, A.K. Tyagi and D.S. Ahlawat, "Influence of pH Variation on Structural and Magnetic Properties of Ni-Zn Ferrite Nanoparticles Synthesized by Auto Combustion Method", Orient. J. Chem., 33(1) (2017) 296-303.
[14] S.H. Lafta, "Effect of pH on Structural, Magnetic and FMR Properties of Hydrothermally Prepared Nano Ni Ferrite", Open Chem., 15(1) (2017) 53-60.
[15] E.M. Elsayed et al., "The effect of solution pH on the electrochemical performance of Nano-crystalline metal ferrites MFe_2O_4 (M= Cu, Zn, and Ni) thin films", Appl. Nanosci., 6(4) (2016) 485-494.
[16] S. Santosh et al., "Effect of Cation Proportion on the Structural and Magnetic Properties of Ni-Zn Ferrites Nano-Size Particles Prepared By Co-Precipitation Technique", Chinese J. Chem. Phys., 21(4) (2008) 381-386.
[17] M.F. Huq et al., "Ni-Cu-Zn Ferrite Research: A Brief Review", J. Sci. Res., 5(2) (2013) 215-234.
[18] B. Shahbahrami et al., "Effect of pH Value on Synthesis and Properties of Zinc Cobalt Ferrite Nano Powders Prepared via Co-Precipitation Method", 15 May 2020, PREPRINT (Version 1) available at Research Square.
[19] S. Hasan and B. Azhdar, "Synthesis of Nickel-Zinc Ferrite Nanoparticles by the Sol-Gel Auto-Combustion Method: Study of Crystal Structural, Cation Distribution, and Magnetic Properties", Adv. Cond. Matter Phys., (2022) Article ID 4603855.
[20] M. Junaid et al., "Structural, spectral, dielectric and magnetic properties of indium substituted copper spinel ferrites synthesized via sol gel technique", Cer. Int., 46(17) (2020) 27410-27418.
[21] P.P. Mohapatra, S. Pittala and P. Dobbidi, "Temperature dependent broadband dielectric, magnetic and electrical studies on $Li_{1-x}Mg_2Fe_{5-x}O_8$ for microwave devices", J. Mater. Res. Technol., 9(3) (2020) 2992-3004.
[22] R. Jose, R. Jothi and N.S.N. Jothi, "Synthesis and characterisation of curcumin loaded $Ag_{(1-x)}Ni_xFe_2O_4$ for drug delivery", Mater. Technol., 36(6) (2021) 339-346.
[23] R.R. Powar, V.D. Phadtare and V.G. Parale, "Effect of zinc substitution on magnesium ferrite nanoparticles: structural, electrical, magnetic, and gas-sensing properties", Mater. Sci. Eng. B, 262 (2020) Article ID 114776.
[24] P.S. Mkwae, I. Kortidis and R.E. Kroon, "Insightful acetone gas sensing behavior of Ce substituted $MgFe_2O_4$ spinel nano-ferrites", J. Mater. Res. Technol., 9(6) (2020) 16252-16269.
[25] K.K. Kefeni, T.A.M Msagati and B.B. Mamba, "Ferrite nanoparticles: synthesis, characterization and applications in electronic device", Mater. Sci. Eng. B, 215 (2017) 37-55.

Numerical Analysis of Electrical Characteristics of Heterojunction AlGaAs/InP Thin Film Solar Cell

Ashwaq T. Dahham[1], Raed M. Humaidan[2], Zuheer N. Majeed[3]

[1] Physics Department, College of Sciences for Woman, University of Baghdad, Baghdad, IRAQ
[2] Salahaddin General Directorate of Education, Tikrit, IRAQ
[3] Physics Department, College of Education for Pure Sciences, Tikrit University, Tikrit, IRAQ

Abstract
High efficiency solar cells are the aim sought by the efforts of researchers due to obtain a clean energy that can face climate changes. In this research a solar cell was designed that contains four layers a window layer emitter layer absorber layer and back surface filed layer. The PCID software was used to simulate the device. Where the effect of thickness and the concentration of doping of window layer was studied within the range 0-1 μm, 10^{17}-10^{20} cm^{-3}, respectively, also the concentration of impurities and value of thickness movables on I-V characteristic of solar cell, and output parameters like I_{SC}, V_{OC} and η. It recorded the best efficiency 30.1% at thickness and doping concentration, 0.02 μm and 1.39×10^{20} cm^{-3}, respectively. The consequence of both of the thickness value and the impurities concentration of the absorbs layer within the area 0-5 μm and 10^{15} cm^{-3} to 10^{20} cm^{-3}, respectively, was also studied. The best values for thickness and doping level were 1.837 μm, and 6.87×10^{15} cm^{-3}, respectively.

Keywords: AlGaAs/InP; Solar cell; Heterojunction, Thin films
Received: 2 March 2020; **Revised:** 5 October 2020; **Accepted:** 12 October 2020; **Published:** 1 January 2021

1. Introduction

All this relating to the production of electric current at the junction (PV) technology converts the solar or light energy into electrical energy without any consumption of conventional form of energy and hence the global photovoltaic market is successful over the decades ago [1]. The main issue of this technology is low conversion ratio of solar energy into electrical form. Prior optimization of various parameters leading to increase in its efficiency is done [2]. III-V compounds have become the basic materials for modern optoelectronic devices. III-V compounds such as gallium arsenide (GaAs), Aluminum Gallium arsenide (AlGaAs), and indium phosphide (InP) have the properties that allow fabrication of high efficiency solar cells. Some of the properties of these materials have direct transmission energy gaps, high optical absorption coefficients, and a suitable note values of minority carrier lifetimes and the mobility [2]. The one - junction solar cell has a limitation in being able to efficiently utilize photons of the broad spectrum from 300 to 2500 nm. As if we say, in the case of (Si) solar cell, it cannot absorb a photon with a wavelength longer than 1100 nm, which accounts for more than 20% of the standard terrene normal radiation at AM1.5 [1], and we must know the wavelengths at the ultraviolet region are not efficiently converted to Si solar because solar cell only converts photons of higher wavelengths than ultraviolet. the stacking solar cells are made by different materials (different power bandgap) together and has proven to be a suitable technique to increase the efficiencies of the solar cells, and several researches groups have proposed several devices made from a stack of single junction cells [2]. Based on the foregoing, two materials in this research with energy gaps close to AlGaAs (1.817eV) and InP (1.35 eV) were selected to obtain a highly efficient solar cell.

2. Numerical Treatment

The PC1D digital simulation way has been use the semiconductor transfer equations as the basic relationships that derived from the

(Boltzmann transformation formula).The values of electrons and holes densities J_n and J_p are calculated by the equations (1) and (2), where μn and μp refers to mobilities of electrons and holes, respectively, and E_{Fn} and E_{Fp} are quasi-Fermi energies for electrons and holes, respectively [3]

$$J_p = \mu_p . p\nabla E_{FP} \quad (1)$$

$$J_n = \mu_n . n\nabla E_{Fn} \quad (2)$$

$$n = N_c e^{-\frac{(E_c - E_{Fn})}{KT}} \quad (3)$$

$$P = N_v e^{-\frac{(E_{Fp} - E_v)}{KT}} \quad (4)$$

In equations (3) and (4), the terms N_C and N_V denote the effective densities of states in both of conduction valence bands. Also, the terms E_c and E_v refer to the conduction band energy and valance band energy.

$$\frac{\partial n}{\partial t} = \frac{\nabla J_n}{q} + G_L - U_n \quad (5)$$

$$\frac{\partial p}{\partial t} = -\frac{\nabla J_p}{q} + G_L - U_p \quad (6)$$

Also, equations (5) and (6) are used to determine the number of charge carriers entering a given volume of space, where U_n refers to the net value for the rate of recombination of electrons, U_p refers to the net value of recombination rate of holes, and G_L refers to created electron-hole pairs in a certain size because of photogeneration.

The term of fill factor (FF) can be defined as the ratio between maximum produced power by solar cell and the product of multiplication between open circuit voltage and short circuit current [4] and given as

$$FF(\%) = \frac{V_{oc} - \ln(V_{oc} + 0.72)}{V_{oc} + 1} \quad (7)$$

The conversion efficiency (η) can be calculated by [4]

$$\eta = \frac{V_{oc} \times I_{sc} \times FF}{P_{in}} \quad (8)$$

The cell photogeneration process can be described by applying the following equation:

$$G = \alpha N_o e^{-\alpha x} \quad (9)$$

where N_0 is the flux of photons on the surface, x is the distance of photon way inside the material, α is the absorption coefficient

The in-cell model uses the Shockley-Reading-Hall formula with different charge carriers' lifetimes and a trap energy level that could be adjusted inside the band gap. Shockley-Reading-Hall formula is given as

$$R = \frac{pn - n_i^2}{\tau_{n0}\left(p + n_i e^{-\frac{E_t}{KT}}\right) + \tau_{po}\left(n + n_i e^{\frac{E_t}{KT}}\right)} \quad (10)$$

where n_i is the concentration of effective intrinsic carrier, τ_{n0} is the electron bulk lifetime, τ_{p0} is the hole bulk lifetime, and E_t is the level of trap energy

3. Methodology

PC1D (One-Dimensional Personal Computer) digital simulation software is widely used in solar cell simulation. This program was developed at South Wales University, Sydney (Australia). It simulates the behavior of the structure of semiconductor solar cells by respecting one dimension (axial symmetry) [5]. In fact, we have run many simulations to see the effect of different factors on solar energy efficiency cells. In this research, a four layer solar cell designed, from n-AlGaAs as a window layer, n-InP emitter layer, p-InP as a base layer and p-AlGaAs as a back surface filed (BSF) layer as shown in Fig. (1).

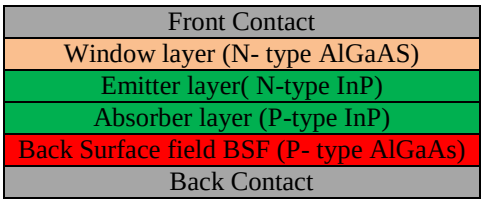

Fig. (1) Device structure of AlGaAs/InP solar cell

In order to obtained highest efficiency of solar cell by studding the effect of thickness and concentration of impurities for window and base. Value of window layer thickness was subsequently changed from 0 to1 μm by icon batch in PCID program, while other parameters were kept constant. Absorber layer thickness was subsequently varied from 0 to 5 μm while other parameters were kept constant. Back ground doping for window and base layers were varied from 10^{17} to 10^{20} cm^{-3} and from 10^{15} to 10^{20} cm^{-3}, respectively.

Through the simulation of the AlGaAs/InP solar cell, and using the parameters shown in table (1) and using PC1D program, the optimal values for both thickness and doping concentration were obtained.

Table (1) parameters using in simulation of solar cell by PC1D

Process Parameters	Value
Device area	1 cm^2
window layer thickness n-(AlGaAs)	0.020 µm
Emitter layer thickness n-(InP)	0.102 µm
Absorber layer thickness p-(InP)	1.837µm
BSF layer thickness p-(AlGaAs)	0.04 µm
Doping concentration of n-AlGaAs	$1.39\times10^{19}cm^{-3}$
Doping concentration of n-InP	$1\times10^{14}cm^{-3}$
Doping concentration of p-InP	$6.87\times10^{15}cm^{-3}$
Doping concentration of p-AlGaAs	$3.91\times10^{15}cm^{-3}$
Energy band gap of AlGaAs	1.817 eV
Energy band gap of InP	1.35 eV
Fundamental concentration for AlGaAs at 300K	1754 cm^{-3}
Fundamental concentration for InP at 300K	$8\times10^{6}cm^{-3}$
Refractive indicator of AlGaAs	3.81
Refractive indicator of InP	3.45
Bulk the process of combining things	$\tau_n=\tau_p=1000\mu s$
Temperature of device	25°C
Primary light exporter	AM 1.5G
Excitement Mode	Transient
Base loop	Sweep from -8 to 5V

4. Results and Discussion

After inserting the input parameters of the structure n-AlGaAs/n-InP/p-InP/p-AlGaAs, the obtained I-V curve is represented in Fig. (2). The open-circuit voltage (V_{OC}), short-circuit current (I_{SC}), and maximum power (P_{max}) in simulation are used to calculate the fill factor and solar cell efficiency. Photovoltaic simulation result under standard test conditions, temperature 25°C, radiation 0.1 mW/cm^2, and AM1.5G, as shown in Fig. (2). With this condition, the current I_{SC} is 32.8 mA, voltage V_{OC} is 1.038V, maximum power is 0.0301W with fill factor (FF) of 88.5% and efficiency of 30.1%.

To investigate the effect that can have the window layer AlGaAs on the overall solar cell performance, some factors, like thickness and doping concentration levels have been changed from 0 µm to 1 µm and from 2.02×10^{17} to 10^{20} cm^{-3}, respectively. Figure (3) shows the relationship between the short-circuit current and the open-circuit voltage with the window layer thickness. We note that the short-circuit current gradually decreased from 32.76 to 18.74 mA with increasing thickness of the window layer from 0 to 1 µm and the highest value of I_{SC} was 32.76 mA at thickness of 0.02 µm. The V_{OC} was 1.0379 V and then decreased slightly to 1.023 V with increasing light layer. The highest value of the conversion efficiency was 30.1% at window thickness of 0.02 µm, then it gradually decreased with increasing thickness of window layer.

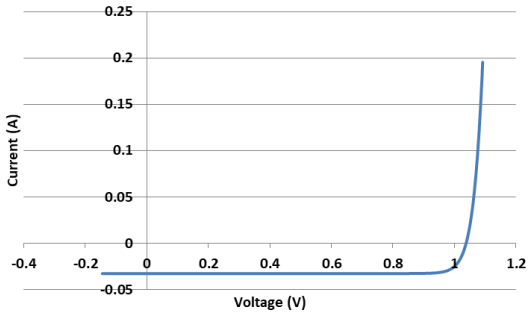

Fig. (2) Current-voltage curve of a typical solar cell

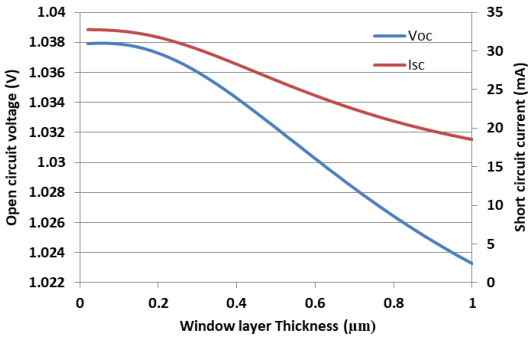

Fig. (3) Variation of open-circuit voltage and short-circuit current as a function of window layer thickness

The results of quantum efficiency express a great value for assembling analysis losses in summing the absorption and optical losses in the structure of window layer. The external quantum efficiency (EQE) is defined as the ratio between number of carriers and the number of energy photons incident on the solar cell. The value of EQE is calculated by [9]

$$EQE(\lambda) = \frac{hc}{q\lambda} SR(\lambda) = \left(\frac{hc}{q\lambda}\right)\left(\frac{J(\lambda)}{E_{e,\lambda}}\right) \quad (11)$$

here, c refers to light velocity, $E_{e,\lambda}$ is the irradiance spectral [$W.m^{-2}.nm^{-1}$], $J(\lambda)$ is the diversion qualification as a duty

Figure (10) depicts the EQE versus wavelength for different values of absorbing layer thicknesses ranging from 0.1 to 2 µm. It can be seen that a decrease in the absorption layer thickness leads to reduce the absorption of photon with longer wavelengths. This is due to the small number of photogenerated electron-hole pairs within the absorbing layer. Moreover, when the wavelength is longer than 930 nm, the EQE drops to zero as no light is absorbed within bandgaps at longer wavelengths and lower energy [10].

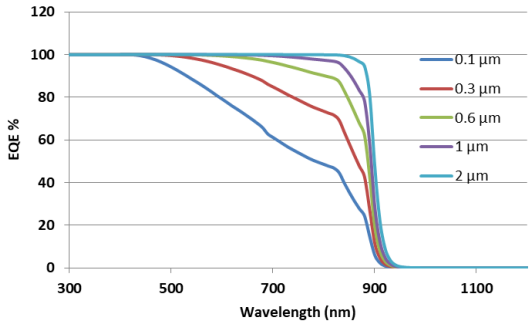

Fig. (10) Variation of EQE as a function of the wavelength

5. Conclusion

In this work, a four-layer solar cell is designed by PC1D program to consist of n-AlGaAs window layer, n-InP emitter layer, p-InP absorber layer and p-type back surface field layer. The thickness and doping level in the window and absorber layer were varied and their effects on solar cell output parameters were studied. After performing the simulation and determining optimum parameters for each layer, the following results were obtained I_{SC}=32.8mA, V_{OC}=1.038V, F.F=88.5% and η=30.1%.

References

[1] M.Z. Rahman and S.I. Khan, "Advances in surface passivation of c-Si solar cells", Mater. Renew. Sustain. Energy, 1(1) (2012), doi: 10.1007/s40243-012-0001-y.

[2] P. Jha and V. Tiwari, "Design and degradation performance analysis of a 3 junction solar cell using PC1D", Int. J. Adv. Eng. Res. Dev., 5 (2018) 2348-6406.

[3] G.S. Thirunavukkarasu et al. "Optimization of Mono-Crystalline Silicon Solar Cell Devices Using PC1D Simulation", Energies, 14 (2021) 4986.

[4] N.R. Paudel, K.A. Wieland and A.D. Compaan, "Ultrathin CdS/CdTe solar cells by sputtering", Solar Energy Mater. Solar Cells, 105 (2012) 109-112.

[5] M. Belarble, A. Benyoucef and B. Benyoucef, "Simulation of the solar cell with pc1d application to cells based on silicon", Adv. Energy: Int. J. (AEIJ), 1(3) (2014).

[6] C.F Kamdem et al., "Study of the Role of Window layer AlGaAs on GaAs –based solar Cells Performance", India J. Sci. Technol., 12(37) (2019).

[7] P. Lin et al., "Numerical Simulation of Cu_2ZnSnS_4 Based Solar Cells with In_2S_3 Buffer Layers by SCAPS-1D", J. Appl. Sci. Eng., 17(4) (2014) 383-390.

[8] K.C. Devendra et al. "Modeling and simulation of AlGaAs/GaAs Solar Cell", Amer. J. Eng. Res., 9 (2020) 218-223.

[9] F. Larsson, "Window layer structure for chalcopyrite thin film solar cells", Ph.D thesis, Uppsala University (2020).

[10] H. Sabbah, "Numerical Simulation of 30% Efficient Lead-Free Perovskite $CsSnGeI_3$-Based Solar Cells", Materials, 15 (2022) 3229.

Theoretical Analysis of Radiation Dose for Gamma Rays in Tissue Equivalent Materials

Mohsin H. Ali

Department of Physics, College of Education for Pure Sciences, Tikrit University, Tikrit, IRAQ

Abstract

In this paper, γ-rays energies at 60, 662, 186, 242, 295, 352, 609, 1120, 1765 keV emitted from radioactive sources (124Am, 137Cs, 226Ra) were used to determinate the radiation dose and attenuation coefficients for samples of different composition prepared from organic compounds (paraffin wax) and sodium chloride. The measurements were made using a gamma ray spectrometer. It is linked to sodium Iodide detector (NaI(Tl)). The obtained results were compared with the ICRU 44 report values. It was found that there is good agreement between these results and that the values of difference is less than 7%. Compared to ICRU 44, this confirms that the materials used in this study are a good alternative for dosimetry and potentially a good alternative material for tissues to make tissue phantoms for the biological tissues studied.

Keywords: Radiation dose; Attenuation coefficients; Gamma radiation; Sodium iodide detector; Exposure rate
Received: 22 May 2020; **Revised:** 22 June 2020; **Accepted:** 22 August 2020; **Published:** 1 January 2021

1. Introduction

In the medical, sciences and biological field, study of γ-ray interaction is very important to calculate radiation dose rate received by the organic compounds and distinguish other parameters of interaction for example mass attenuation coefficients in organic tissues for example soft and bone-tissues . The γ-ray energy in keV are very interest in therapy and medical diagnosis as well as in radiation biology. Different materials have been utilized to mimic human-tissues to determine rate radiation dose to patients exposed for high energy radiations. These organic compounds are called tissue-equivalent materials [1–5]. The attenuation of radiation, which usually occurs in tissues, one of most significant studies of gamma radiation in nuclear treatment. Therefore, attenuation coefficients represent the possibility of interaction between radiation and matter. Attenuation of radiation in a substance per unit length is known as the linear attenuation coefficient. Mass attenuation coefficients ($\frac{\mu}{\rho}$) are of great importance through the absorption of radiation by materials which can study some basic atomic parameters such as radiation dosimetry [6 - 11]. Radiation therapy methods depend on the absorption or scattering of the incident radiation by the body's organs, tissues and bones, and therefore radiology techniques give anatomical images depending on the physical characteristics of the body tissues. Where it was found by studying the differences in tissue patterns to describe genes when exposed to a constant radiation dose to be completely uniform and equal [12-15]. Tissue exposure to high radiation doses is unacceptable for patients with radiotherapy problems, as this can be reduced by good approximation of tissue type and thickness when radiation passes through and careful selection of radiopharmaceutical sources [16, 17]. The exact values of material attenuation coefficients are very important basic parameters in various scientific fields such as nuclear physics and radiological physics [18-20].

2. Theoretical and Methods

The radionuclide efficacy is a measure of the intensity of the radiation emitted during radioactive decay, and is defined in the following equation [21, 22]:

$$A_i = -dN_i / dt = \lambda_i N_i \cdots (1)$$

A_i, It is the effectiveness of the isotope of a radioactive source, equal to the number of radioactive decay nuclei dN_i at a given time (dt) and proportional to the number of radioactive nuclei N_i at the moment (t), λ_i is the decay constant. The half-life (t1/2) associated with the decay constant is given by the following relationship [23]:

$t_{1/2} = \ln 2 / \lambda_i \cdots(2)$

and the solution to the equation (1) is given as follows [24]:

$N_i = N_0 e^{-\lambda t} \cdots(3)$

N_0 the number of nuclei at a time (t=0) and N_i is the number of nuclei at a time (t). The above equation can be written in terms of radioactivity in the following form [24]:

$A_i = A_0 e^{-\lambda t} \cdots(4)$

A_0 is initial nucleus activity in time (t=0) and A_i is final nucleus activity at time (t). The minus sign indicates the fact that radioactivity decreases with time.

When ionizing radiation penetrates a substance, such as the human body, it deposits energy with it. Absorbed energy each unit mass of radiation exposure is called a dose. And the concept of dose may mean (dose absorbed, equivalent dose, equivalent effective dose). The radiative forcing occurs only when transmitted energy from radiation to some material being irradiated, and possibly the radiative effect is different when a certain amount of energy is added to a small mass of matter instead of distributing energy over a large mass. The change in energy absorbed (ΔE) per unit mass (m) called the absorbed radiation dose is measured in (Gray) units, as in the following equation [25]:

$D = \Delta E / m \cdots(5)$

As for the dose-rate, it represents the radiation dose per unit time ($Gray/h\,r$).

As in a given material medium, each photon in the beam is either completely removed from the beam by scattering or absorption, and this leads to an exponential weakening of the beam proportional to the thickness of the absorbing medium to the package or not interacting with the physical medium at all. The attenuation of a beam of gamma rays may be the attenuation of its energy or the attenuation of its intensity along the path through the medium [26].

The dose rate for a symmetric point radioactive source is given by the following relationship [27]:

$D' = De^{-\mu x} \cdots(6)$

$D = \Gamma A_i / d^2 \cdots(7)$

Γ the fixed dose rate and (d) the distance between radiating source and the detector , where the factor $\frac{\Gamma A_i}{d^2}$ is called exposure rate.

Since the rate of radiation dose in units (μSv/hr) can be calculated using the following relationship [28]:

$$D = 0.142 \times A_i/d^2 \times \sum_i f \times E_\gamma \ (8)$$

(f) is ratio of number of gamma-ray emitted with a specific energy of line per (100) decay of the decay of the radioactive isotope and E_γ the energy of incident gamma ray.

When calculating the total radiation dose rate ($D't$) for a radioactive source that contains more than Energy we use the following relationship [28]:

$$D'_t = \sum_i D' \ (9)$$

Attenuation of Radiation of transmitted by a medium can be describe through Beer-Lambert law [29]:

$$I/I_0 = e^{-(\mu \times x)} \qquad (10)$$

$$\mu = (\ln(I_0/I)/x) \qquad (11)$$

$$(I/I_0) = e^{-(\mu/\rho \times \rho x)} \qquad (12)$$

$$\mu/\rho = (\ln I_0/I/(\rho x)) \qquad (13)$$

I and I_0 is initial intensity of the radiation and the intensity of the attenuated radiation respectively , where x is thickness of absorption material, μ is linear attenuation coefficient in (cm^{-1}), Therefore, from Eq. (11) when dividing it by the density of the samples, we get the mass attenuation coefficient

$$\mu/\rho = ((\ln I_0/I)/\rho x) \qquad (14)$$

ρ is density of material.

3. Results and Discussion

The coefficients of attenuation and radiation dose of the equivalent materials for the prepared tissues were found. The results are shown in Tables (1) and (2), and the

difference values between the mass attenuation coefficients and the ICRU–44 [30] was calculated. It was noted that the differences are less than 7%, and this confirms the possibility of using these prepared materials as equivalent materials for tissues as an alternative to smooth and hard tissues that are used in nuclear medicine and radiotherapy.

Table (1) Attenuation coefficients, and radiation dose ($\mu Sv/hr$) of A and B samples

E keV	60	186	242	295	352	609	662	1120	1765
μ ×10^{-2}	20	13	12	11	10	8.2	8	7	5.4
μ_m ×10^{-2}	18	12	11	10	9	8	7	6	5
D' ×10^{-4}	76	217	22	223	23	236	610	24	25

Table (2) Attenuation coefficients, and radiation dose ($\mu Sv/hr$) of C and D samples

E keV	60	186	242	295	352	609	662	1120	1765
μ ×10^{-2}	44	30	26	24	22	19	18	14	12
μ_m ×10^{-2}	31	21	18	17	15	14	13	10	8
D' ×10^{-4}	67	212	215	219	225	226	547	231	235

Also, the radiation dose was found for all the prepared samples, and it was noted that the radiation dose decreases with the increase in the concentration of the additive, while the radiation dose increases with the increase in the energy of gamma rays, as well as with the increase in the radioactivity of the radioactive source, as shown in figures (8) and (9). It was found that there is a good agreement between the experimental values and the values of ICRU-44. The study demonstrated the possibility of using these prepared materials as alternative tissue equivalent materials for smooth and hard tissues that are used in nuclear medicine and radiotherapy.

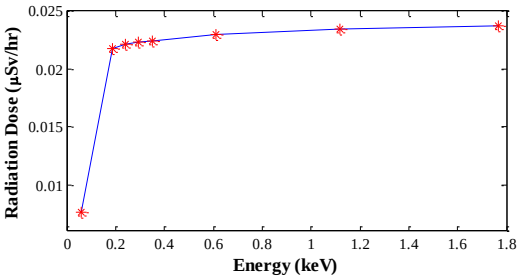

Fig. (8) Radiation dose of A and B samples

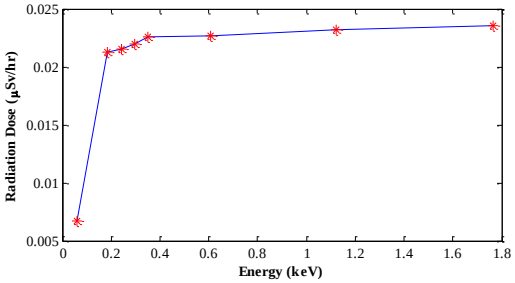

Fig. (9) Radiation dose of C and D samples

4. Conclusion

The values of the mass attenuation coefficients depend on the physical and chemical composition of the atomic elements that make up the sample. It was found that these values of the attenuation coefficients decrease for all samples when the energy of the gamma rays increases. The difference between the obtained values and the practical values is less than 7%. Therefore, these parameters improve our understanding of how the attenuation coefficients change with different atomic number, electronic density, and percentage of additive to organic matter. This study also demonstrates the possibility of using the prepared material to provide tissue equivalents for phantom fabrication.

References

[1] A. K. Jones, D. E. Hintenlang, and W. E. Bolch, Tissue-equivalent materials for construction of tomographic dosimetry phantoms in pediatric radiology, Med Phys, (2003).

[2] I. Amini, P. Akhlaghi, and P. Sarbakhsh, Construction and verification of a physical chest phantom from suitable tissue equivalent materials for computed tomography examinations, Radiat Phys Chem, (2018).

[3] N. A. B. Amin, N. J. Abualroos, and R. Zainon, Fabrication of anthropomorphic thyroid-neck phantom for dosimetry study in nuclear medicine., Radiat Phys Chem, (2020).

[4] D. Chandramohan et al., Bone material analogues for PET/MRI phantoms, Med Phys, (2020).
[5] G. Singh, M. K. Gupta, A. S. Dhaliwal, and K. S. Kahlon, Measurement of attenuation coefficient, effective atomic number and electron density of oxides of lanthanides by using simplified ATM-method, J Alloys Compd, (2015).
[6] A. Frimaio, B. C. Nascimento, R. M. M. Barrio, L. L. Campos, and P. R. Costa, X-ray spectrometry applied for determination of linear attenuation coefficient of tissue-equivalent materials, Radiat Phys Chem, (2019).
[7] M. Büyükyıldız and M. Kurudirek, Radiological properties of healthy, carcinoma and equivalent breast tissues for photon and charged particle interactions, Int J Radiat Biol, (2018).
[8] I. Jarrah, M. I. Radaideh, and T. Kozlowski, Determination and validation of photon energy absorption buildup factor in human tissues using Monte Carlo simulation, Radiat Phys Chem, (2019).
[9] V. P. Singh, S. P. Shirmardi, R. Bagheri, R. Adeli, and M. Tatari, A case study of energy absorption buildup factors in some human bones for gamma energies 30 keV to 1.5 MeV, Arch Adv Biosci, (2017).
[10] H. Hadi and A. Ali, Introducing a simple tissue equivalent anthropomorphic phantom for radiation dosimetry in diagnostic radiology and radiotherapy, (2011).
[11] O. Kadri and A. Alfuraih, Photon energy absorption and exposure buildup factors for deep penetration in human tissues, Nucl Sci Tech, (2019).
[12] J. Coulaud et al., Tissue-inspired phantoms: a new range of equivalent tissue simulating breast, cortical bone and lung tissue, Biomed Phys Eng Express, (2018).
[13] G. Apaza, F. Chen, and J. Vega, Construction and characterization of materials equivalent to the tissues and organs of the human body for radiotherapy, Radiat Phys Chem, (2019).
[14] D. R. White, The design and manufacture of anthropomorphic phantoms, Radiat Prot Dosimetry, (1993).
[15] M. M. Rafiei and H. Tavakoli-Anbaran, Calculation of the exposure buildup factors for x-ray photons with continuous energy spectrum using Monte Carlo code, J Radiol Prot, (2018).
[16] K. Maeda, M. Matsumoto, and A. Taniguchi, Compton-scattering measurement of diagnostic x-ray spectrum using high-resolution Schottky CdTe detector, Med Phys, (2005).
[17] M. Kurudirek and Y. Kurucu, Estimation of energy absorption buildup factors of some human tissues at energies relevant to brachytherapy and external beam radiotherapy, Int J Radiat Biol, (2019).
[18] I. O. Olarinoye, Photon buildup factors for some tissues and phantom materials for penetration depths up to 100 MFP, (2017).
[19] O. Kadri, K. Manai, and A. Alfuraih, Monte Carlo study of the cardiac absorbed dose during X-ray examination of an adult patient, Radiat Prot Dosimetry, (2016).
[20] N. A. M. Alsaif et al., Calculating photon buildup factors in determining the γ-ray shielding effectiveness of some materials susceptible to be used for the conception of neutrons and γ-ray shielding, J Mater Res Technol, (2021).
[21] S. M. Seltzer et al., Fundamental quantities and units for ionizing radiation, ICRU J, (2011).
[22] N. Chanthima et al., Development of BaO–ZnO–B2O3 glasses as a radiation shielding material, Radiat Phys Chem, (2017).
[23] M. P. Silverman, Search for non-standard radioactive decay based on distribution of activities, EPL (Europhysics Lett, (2015).
[24] I. Nsiah-Akoto, J. J. Fletcher, O. C. Oppon, and A. B. Andam, Indoor radon levels and the associated effective dose rate determination at Dome in the Greater Accra Region of Ghana, Res J Environ Earth Sci, (2011).
[25] N. Tsoulfanidis and S. Landsberger, Measurement & detection of radiation. CRC press, 2021.
[26] M. G. Stabin, Fundamentals of nuclear medicine dosimetry. Springer Science & Business Media, 2008.
[27] H. A. Shousha, N. Rabie, and G. M. Hassan, Experimental investigation of commercially available lead composite aprons used for diagnostic X-rays, Radiat Eff Defects Solids, (2011).
[28] N. E. Bolus, Basic review of radiation biology and terminology, J Nucl Med Technol, (2001).
[29] C. T. Chantler, C. Q. Tran, Z. Barnea, D. Paterson, D. J. Cookson, and D. X. Balaic, Measurement of the x-ray mass attenuation coefficient of copper using 8.85–20 keV synchrotron radiation, Phys Rev A, (2001).
[30] ICRU 1989, 'ICRU Report 44',International Commission on Radiation Units and Measurements Bethesda, MD, USA.

Effect of Acidity Environment on Synthesis of $Ni_{0.5}Zn_{0.5}Fe_2O_4$ by Co-Precipitation Method

Abdulsamee F. Abdul Aziz, Najat A. Dahham, Omar F. Fouad

Department of Physics, College of Science, University of Tikrit, Tikrit, IRAQ

Abstract

$Zn_{0.5}Ni_{0.5}Fe_2O_4$ nanocomposites have been prepared by a simple co-precipitation method. The prepared samples were characterized by powder x-ray diffraction (XRD) and scanning electron microscopy (SEM) after analysis it found that with increasing the PH value for the nickel-zinc ferret the grain size decrease with increase the concertation of zinc content also it found the morphology of the simple also effected by adding different concentration for pH.

Keywords: Nonmagnetic material; Chemical co-precipitation; Zinc ferrite; Nickel ferrite
Received: 2 May 2020; **Revised:** 5 July 2020; **Accepted:** 4 November 2020; **Published:** 1 January 2021

1. Introduction

Nowadays, spinel type magnetic metal oxide nanoparticles (NPs) have attracted significant attention in many areas such as ceramics, semiconductors, sensors and catalytic materials, due to their unique dielectric, magnetic, and optical properties, Nano-crystalline ferrites are materials of great interest from both a scientific and technological standpoint [1-2]. Due to the interaction of quantum, finite-size, surface, and interfacial effects, these magnetic materials serve as the foundation for a very active area of research. New phenomena are occurring at the nanoscale, and these phenomena are the result of this interaction. Spinel ferrite nanoparticles have numerous technical applications in a variety of fields, including hyperthermia, magnetic separation, magnetic resonance imaging, high-density information storage, Ferro fluids, catalysts, drug targeting, and magnetic separation [3]. The critical inquiries in these frameworks are the manner by which these Nano-structures adjust their attractive and electronic properties and how one can exploit those new properties to work on the applications. Subsequently, understanding and controlling the impacts of the nanostructures on the properties of the particles have become progressively significant issues for innovative applications [4].

In the present work, synthesis of $ZnFe_2O_4$ nanoparticles was carried out by chemical co-precipitation method. Synthesized NiZn-ferrite nanoparticles were characterized by standard characterization techniques to study the structural and morphology of surface.

2. Experimental Work

To prepare the compounds used in work by chemical precipitation method, iron nitrate, zinc nitrate and nickel nitrate were dissolved in (100ml) of distilled water using a magnetic stirrer (Stirrer magnetic) at a temperature of (60°C) and for half an hour in order for the substance to be completely and homogeneously dissolved in distilled water, then all the solutions are mixed in a glass flask at a temperature of (60°C) for half an hour with continuous stirring by means of the magnetic mixer. As for the second stage, (40g) of sodium hydroxide (NaOH) was dissolved in (200 ml) of distilled water in a glass flask with continuous stirring using a magnetic mixer at a temperature of (60°C) for 15 min. Sodium hydroxide solution is used as a precipitating agent and to determine the pH value. As for the third stage, it included mixing all the solutions in a glass flask at a temperature of (60°C) for half an hour with continuous stirring by means of the magnetic mixer. Then we distill the sodium hydroxide solution mixture by a burette slowly over the

solution of the mixture of solutions while continuing the mixing process at a temperature (60°C) until the sodium hydroxide solution is distilled to determine the pH value. After completing the distillation process, the solution will be clear with a pH that we determine. This solution is filtered with filter paper and then washed several times with distilled water to get rid of insoluble nitrates. Then the resulting substance is taken and dried in a drying oven at a temperature (100°C) to obtain a dry moisture-free compound. Then the powder we obtained is calcined at a temperature of (700°C) for 2 hours.

3. Results and Discussion

The ferrite samples were prepared based on the molar concentration and molecular weights by comparing the x-ray diffraction patterns of ferrite after sintering at a temperature of 700°C and in comparison with the standard labels it was found that they are identical to the standard label number (JCPDS 8-324) and as shown in Fig. (1) x-ray diffraction spectrum of $Ni_{0.5}Zn_{0.5}Fe_2O_4$ with a pH number (pH=1.8, 7, 10) and the appearance of peaks(220), (311), (222), (400), (422), (333), (440), (533) within the angular range (20°-80°) for all the compounds prepared by chemical precipitation method, where the peaks are considered dominant, which refers to the geometric crystal structure of ferrite powder and from Observe the shape of the diffraction spectrum, the appearance of the spin phase of zinc [5-6]. No impurities were found for any other material, which proves that the material has a very high purity.

The morphology and the size distribution of the $Ni_{0.5}Zn_{0.5}Fe_2O_4$ nanoparticles were determined using SEM. Typical SEM images of $NiFe_2O_4$ synthesized as for the sample with the structural formula Figure (2) shows the $Ni_{0.5}Zn_{0.5}Fe_2O_4$ prepared by the method prepared at different pH values, as the results showed that the grain size changes (32-55 nm) and is relatively regular, and this is consistent with the results of X-ray diffraction, as the results showed that the particles of the sample $Ni_{0.5}Zn_{0.5}Fe_2O_4$ consist of nanoclusters.

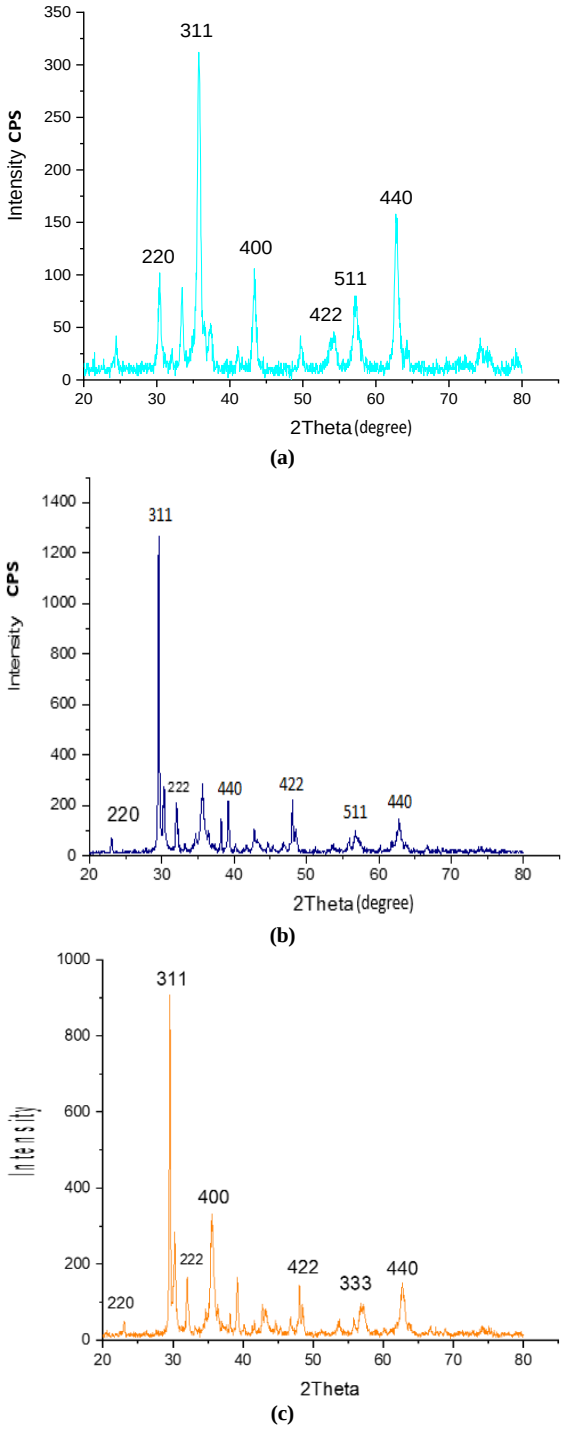

Fig. (1) XRD patterns of $Ni_{0.5}Zn_{0.5}Fe_2O_4$ at different values of pH (1.8, 7 and 10)

The presence of small particles and the presence of these assemblies is evidence of the presence of crystals free of pores on the resulting surface and also found that they have a strong tendency to stick together and form clumps, due to magnetic interactions between particles of ferrite materials during the

preparation process and this is consistent with what the researcher said [6-8].

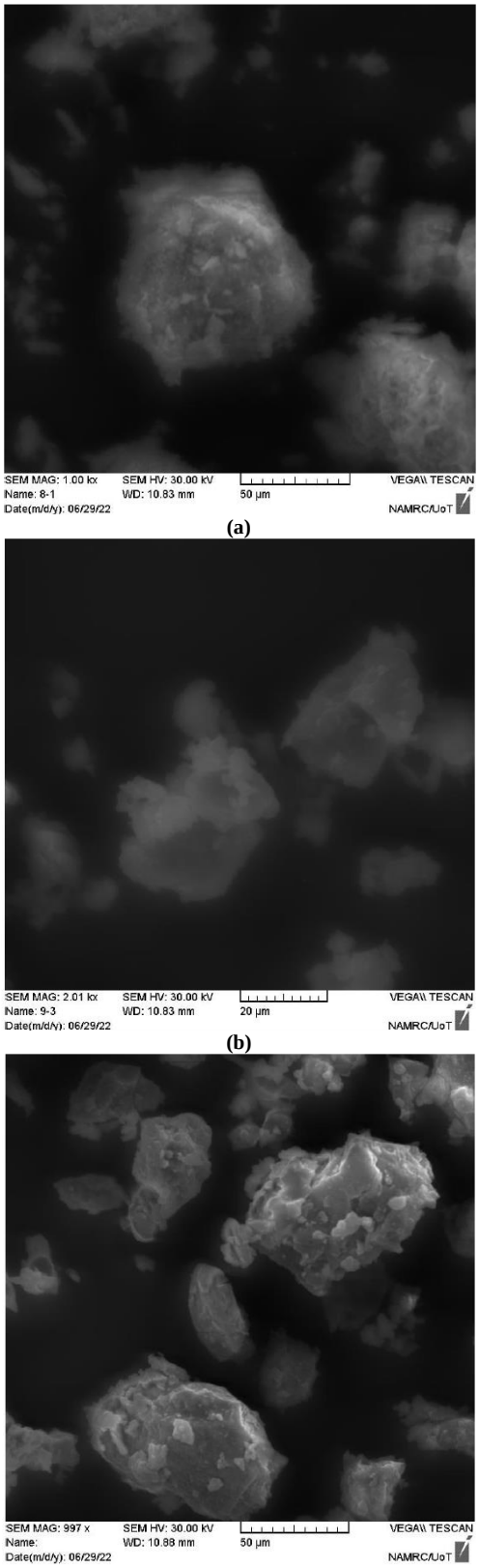

Fig. (2) SEM images of $Ni_{0.5}Zn_{0.5}Fe_2O_4$ at different values of pH (1.8, 7 and 10)

It was also noted that the nanoparticles are in larger sizes the higher the pH of the solution there are also some voids in the prepared sample and this may be due to the interaction between magnetic nanoparticles and thus these particles grow to some extent to form larger particles at a high pH of the solution. (1.8 to 10). The reason for the increase in the granular size of ferrite materials is due to the fact that magnetic materials tend to agglomerate, which leads to the gathering of particles with each other, which leads to an increase in the surface area of the material Thus, the granule size increases. We can also justify this increase due to the recrystallization that reduced the amplitude of the lattice constant [9-10].

4. Conclusion

$Ni_{0.5}Zn_{0.5}Fe_2O_4$ nanoparticles using Co-precipitation chemical routes were successfully synthesized with an ideal structure. XRD pattern showed the cubic spinel structure of Fd3m space group. Further, observed that the particle size of sample prepared by the co-precipitation method is very small. Thus, it is concluded that the co-precipitation is a better route for the synthesis of fine Zinc ferrite nanoparticles.

References

[1] W.D. Kingly, D.R. Uhmann and H.K. Bowen, **"Introduction to Ceramic"**, 2nd ed., John Wiley & Sons (NY, 1976).
[2] P.I.B. Clarricoats, **"Microwave Ferrites"**, Chapman & Hall Ltd. (London, 1961).
[3] C. Kittle, **"Introduction to Solid State Physics"**, 5th ed., John Wiley & Sons (NY, 1976).
[4] K.J. Standley, **"Oxide Magnetic Materials"**, 2nd ed., Clarendon Press (Oxford, 1972).
[5] L.L. Hench and J.K. West, **"Principle of Electronic Ceramic"**, John Wily & Sons (1990).
[6] M.M Eltabey, W.R. Ajami and H.T. Mohsen, "Improvement of the magnetic properties for Mn-Ni-Zn ferrites by rarearthe Nd^{2+} ion substation", J. Adv. Res., 5 (2014) 601-605.
[7] V.A. Goel et al., "High resistivity nickel-zinc ferrites by the citrate precursor method", J. Magnet. Mater., 192 (1999) 271-276.
[8] O.A. Hammadi, M.K. Khalaf and F.J. Kadhim, "Fabrication of UV Photodetector from Nickel Oxide Nanoparticles Deposited on Silicon Substrate by Closed-Field Unbalanced Dual

Magnetron Sputtering Techniques", Opt. Quantum Electron., 47(12) (2015) 3805-3813.

[9] G.H. Jonker and A.L. Stuijts, "Controlling the properties of electroceramic materials through their microstructure", Philips Tech. Rev., 32(3/4) (1971) 79-95.

[10] A.L. Stuijts and C. Kooy, "Influence of Technological Factors on the Sintering Behavior of ferrite", in Proc. Conf. held under the auspices of British Cer. Soc. and the Netherlands Keramische Vereniging at Noordwijk an Zee 13-17 May, 1963, in Science of Ceramic, edited by G.H. Stewart, v2 (1965).

[11] R.H. Turki and M.A. Hameed, "Spectral and Electrical Characteristics of Nanostructured NiO/TiO_2 Heterojunction Fabricated by DC Reactive Magnetron Sputtering", Iraqi J. Appl. Phys., 16(3) (2020) 39-42.

[12] G.A. Hossienpour et al., "Electromagnetic properties and microwave absorbing characteristics of doped barium hexaferrite", J. Magnet. Mag. Mater., 302 (2006) 429-435.

[13] O.A. Hammadi and N.E. Naji, "Fabrication and Characterization of Polycrystalline Nickel Cobaltite Nanostructures Prepared by Plasma Sputtering as Gas Sensor", Phot. Sen., 8(1) (2018) 43-47.

IRAQI JOURNAL OF APPLIED PHYSICS LETTERS
EDITORIAL BOARD

COPYRIGHT RELEASE FORM

IRAQI JOURNAL OF
APPLIED PHYSICS LETTERS (IJAPLett)

We, the undersigned, the author/authors of the article titled

……
……
……
……
……
……
……

that is submitted to the Iraqi Journal of Applied Physics Letters (IJAPLett) for publication, declare that we have neither taken part or full text from any published work by others, nor presented or published it elsewhere in any other journal. We also declare transferring copyrights and conduct of this article to the Iraqi Journal of Applied Physics Letters (IJAPLett) after accepting it for publication.

The authors will keep the following rights:

1. Possession of the article such as patent rights.
2. Free of charge use of the article or part of it in any future work by the authors such as books and lecture notes after informing IJAP editorial board.
3. Republishing the article for any personal purposes of the authors after taking journal permission.

To be signed by all authors:

Signature:……..date: ……
Printed name: ……

Signature:……..date: ……
Printed name: ……

Signature:……..date: ……
Printed name: ……

Correspondence author:……...
……
Address:……
……
Telephone:……..……..email: ……

Note: Complete and sign this form and mail it to the below address with your finally revised manuscript

The Iraqi Journal of Applied Physics Letters
ISSN (Print): 1999-656x, ISSN (Online): 2309-1673
www.iraqiphysicsjournal.com
Email: editor@iraqiphysicsjournal.com
Email: editor_ijap@yahoo.co.uk
Email: ijap.editor@gmail.com

IRAQI JOURNAL OF APPLIED PHYSICS LETTERS
Volume (4) Issue (1) January-March 2021

CONTENTS

The *Iraqi Journal of Applied Physics Letters (IJAPLett)* is a peer reviewed journal of high quality devoted to the publication of original research papers from applied physics and their broad range of applications. IJAPLett publishes quality original research letters in physics and its applications in the broadest sense. It is intended that the journal may act as an interdisciplinary forum for physics and its applications. Innovative applications and material that brings together diverse areas of physics are particularly welcome. IJAPLett aims to disseminate knowledge; provide a learned reference in the field; and establish channels of communication between academic and research experts, policy makers and executives in industry, commerce and investment institutions. IJAPLett is a quarterly specialized periodical dedicated to publishing original letters in: Applied & Nonlinear Optics, Applied Mechanics & Thermodynamics, Digital & Optical Communications, Electronic Materials & Devices, Laser Physics & Applications, Plasma Physics & Applications, Quantum Physics & Spectroscopy, Semiconductors & Optoelectronics, Solid State Physics & Applications, Alternative & Renewable Energy, and Environmental Science & Technology.

Sponsored and Published by
Iraqi Society for Alternative and Renewable Energy Sources and Techniques

Co-published by
American Quality for Scientific Publishing